Static Negative-Permeability Metasurface to Transfer Volumetric Static Magnetic Field

Tie Qiu,[1,2,*] Choon Kait Andrew Tek,[2] and Shao Ying Huang[1,3]

[1]*Engineering Product Development Pillar, Singapore University of Technology and Design, 487372, Singapore*
[2]*Electronic Industrial Solutions Group - Centers of Excellence, Keysight Technologies, 768923, Singapore*
[3]*Yong Loo Lin School of Medicine, National University of Singapore, 119228, Singapore*

Inspired by transformation optics, negative permeability materials enable the transfer of static magnetic fields to a distant location far away from the current source. This is useful for situations in which it is difficult to place a current source near the region where magnetic fields are required. However, existing artificial negative permeability materials are three dimensional (3D) and bulky. In this study, we theoretically design and experimentally demonstrate a metasurface with static negative permeability that displaces volumetric 3D magnetic fields to a distant region. The design overcomes the existing limitation because the dimensions of the structure are reduced to two, and the control of the magnetic field has an increased degree of freedom. The proposed method can be further extended to tools and strategies to precisely displace and/or manipulate dc or quasistatic magnetic fields in regions of interest for various applications such as medical care and measurement precision.

I. INTRODUCTION

The manipulation of dynamic or static magnetic fields is applicable in numerous areas, from conventional applications such as power generators [1], transformers [2], and wireless power-transfer devices [3], to biomedical applications that can guide magnetic particles inside the human body for disease treatments [4]. Suitably controlled static magnetic fields can be used to improve the performance of magnetic sensors [5,6], achieve precise drug delivery using magnetic nanoparticles [4,7], improve the image quality in magnetic resonance imaging (MRI) [8,9], etc. Following the introduction of transformation optics techniques [10] and the emergence of metamaterials, advanced magnetic metamaterials have been introduced in the past decade, leading to structures with interesting manipulations of magnetostatic fields, including magnetic cloaks [11–14], magnetic concentrators [12,15–18], magnetic hoses [19, 20], magnetic wormholes [21], magnetic illusion devices [22,23], etc.

Among these magnetic metamaterials, some require a negative permeability to achieve a magnetic illusion that transforms an object into another or magnifies the size of the original object [23,24], or cancels or creates a magnetic source at a distance to achieve precise control of the magnetic field [22,25]. Although resonances from passive

materials or devices can effectively produce negative permeabilities under dynamic conditions [26,27], the same methods could not work under a static condition because of the absence of time-varying magnetic fluxes. To implement a static negative permeability (SNP) metamaterial, in Ref. [28], current sources were proposed to form a spherical shell with a negative permeability, which concentrates the applied magnetic field inside the shell without distorting the fields outside it. Following Ref. [28], a similar technique was applied to achieve a magnetic illusion that transforms a magnetic object into another [23]. Recently, another SNP metamaterial was designed by surrounding a straight current with a group of currents running parallel to it, forming a cylinder, to displace the magnetic field generated by the current inside the cylinder to a distant region [25]. The proposed SNP metamaterial is three-dimensional (3D) and takes up space; thus, it cannot easily be used in real applications.

A two-dimensional (2D) SNP material, that is, an SNP metasurface, is preferred to facilitate a real application; such a design is presented in this work. Here, based on transformation optics, we theoretically and experimentally demonstrate a SNP metasurface that equivalently creates a SNP volume with a relative magnetic permeability $\mu_r = -1$, and can displace a loop current in or outside this volume in its normal direction, behaving analogously to an electromagnetic lens at dc. This is illustrated in Fig. 1, which consists of a set of concentric loops running with dc currents. This SNP metasurface generates an equivalent
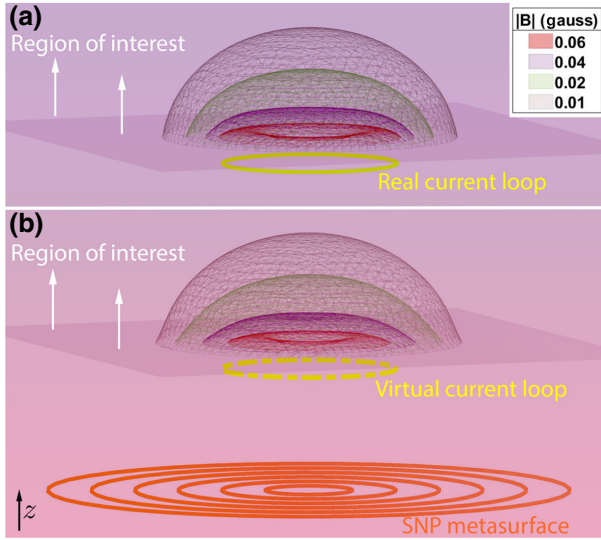
*qiu.tie@keysight.com

FIG. 1. Proposed SNP metasurface composed of concentric current loops generates the virtual current loop close to the ROI in (b), acting as if there is another real current loop nearby as shown in (a).

medium with $\mu_r = -1$ below it such that it can project a virtual coaxial loop current to a position close to the region of interest (ROI) along the axial direction, acting as if there is a real current loop below the ROI.

II. RESULTS AND DISCUSSION

The magnetostatic Maxwell's equations are solved for a cylindrical SNP medium with a thickness of Z_0 ($z = -Z_0 \sim 0$, as shown in Fig. 2), an infinite radius, R, and $\mu_r = -1$ in the cylindrical coordinate system (see details in Appendix A). When a coaxial excitation loop current I_e at $z = -D$ is embedded in the medium (denoted as L_{in}) or placed outside the medium at $z = -2Z_0 + D$ (denoted as L_{ext}), along with the SNP medium, they generate magnetic fields in the ROI ($z > Z_0$), which is the same as that generated by the virtual loop current at $z = D$ (denoted as L_{eq}).

In Fig. 2, both the SNP metasurface at $z = 0$ and the auxiliary currents at $z = -Z_0$ are shown, in between which there is the SNP medium with $\mu_r = -1$. The surface magnetization current densities on the top and bottom surfaces of the SNP medium (which can be emulated by the SNP metasuface and auxiliary currents) are denoted as $\mathbf{K}_t(r)$ and $\mathbf{K}_a(r)$, respectively. Thereafter, the magnetic field in the entire space can be transformed to the summation of the field generated by $\mathbf{K}_t(r)$, $\mathbf{K}_a(r)$, and the excitation current loop L_{in} or L_{ext} in a space of $\mu_r = 1$ (L_{in} generates a magnetic field equivalent to that of a current loop with opposite current direction in the free space); in the ROI, the field generated by the excitation loop cancels with the field generated by $\mathbf{K}_a(r)$. This implies that only the SNP
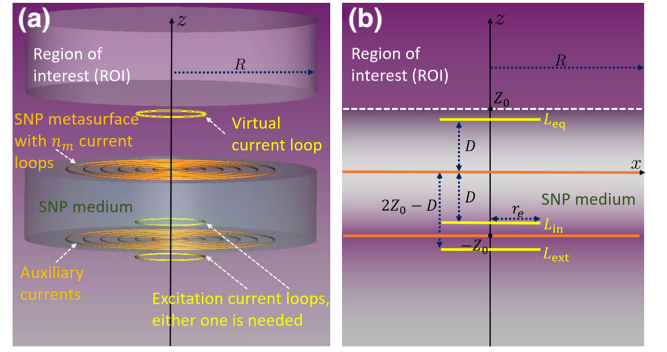

FIG. 2. Detailed illustration of the design of the SNP metasurface: (a) 3D view; (b) 2D side view.

metasurface is required to generate magnetic fields in the ROI. Comparing the SNP metasurface to L_{eq}, a distance of D is gained for the distant generation of fields. $\mathbf{K}_t(r)$ is expressed as follows:

$$\mathbf{K}_t(r) = I_e r_e \int_0^\infty e^{Dt} J_1(r_e t) J_1(rt) t \, dt \hat{\phi}, \qquad (1)$$

where r_e denotes the radius of the excitation loop L_{in} or L_{ext}, and J_1 is the Bessel function of the first kind of order one.

Notably, $\mathbf{K}_t(r)$ is divergent, implying that the exact implementation of a SNP metasurface requires infinite surface current density. Meanwhile, it is oscillating in the r direction. Moreover, if D approaches zero, $\mathbf{K}_t(r)$ in Eq. (1) approximates to L_{in}, implying that the SNP metasurface does not gain any distance for a distant generation of fields. When D increases and approaches Z_0, $\mathbf{K}_t(r)$ increases exponentially, implying that more power is required to generate the field in a distant ROI. In addition, the field solution for the magnetic vector potential in the region $z \in [0, D)$ is divergent, which is similar to the anomalous resonance [29,30]. This divergent region enables the possibility of a divergence of the magnetic field at the virtual current loop position without having a local field maximum in the free space; thus, Earnshaw's theory [31] is not violated. The surface current density at the bottom $\mathbf{K}_a(r)$ has a similar expression, and the diverging or converging behavior depends on the location of the excitation loop. For the thickness Z_0, based on the derivation, it affects only $\mathbf{K}_a(r)$ and is not related to $\mathbf{K}_t(r)$.

Therefore, to physically implement the SNP metasurface and auxiliary currents, $\mathbf{K}_t(r)$ and $\mathbf{K}_a(r)$ are truncated and discretized in the r direction into n_m concentric surface currents by applying numerical approximation and optimization. The truncation and discretization are performed by enforcing the boundary condition at the boundaries of the SNP medium at $z = -Z_0$ and $z = 0$ with preset radii of the n_m concentric surface current loops, as shown in Fig. 2(a). To enforce the boundary condition, the residual

function f for minimization is expressed as follows:

$$f = \sum_{j=1}^{n_c} \left(\sum_{i=1}^{2n_m+1} \frac{B_{t-\text{in}}^{ij}}{\mu_{\text{in}}} - \sum_{i=1}^{2n_m+1} \frac{B_{t-\text{out}}^{ij}}{\mu_{\text{out}}} \right)^2, \quad (2)$$

where B_t denotes the tangential components of the **B** field generated from the surface current loops at the boundary and the excitation loop, μ is the relative magnetic permeability value, and the subscripts in and out denote inside or outside the SNP medium, respectively. In addition, i indexes the current loops, including the excitation current loop L_{in} or L_{ext}, j indexes the observation points on the boundary, and n_c denotes the total number of observation points. For the optimization, **B** of the current loops is calculated based on the closed-form expression in Ref. [32]. Notably, when the excitation loop is L_{in}, the current direction inside it for the optimization should change to the opposite.

To demonstrate the proposed SNP metasurface, Z_0 is set as 10 mm, targeted in a ROI at $z > 10$ mm. The excitation loop current (with a radius of 10 mm) is placed 3 mm above or below the bottom surface, that is, $D = 7$ mm to create an equivalent current loop at $z = D = 7$ mm, and I_e is set as 0.1 A. The number of concentric current loops of the SNP metasurface, n_m, is set as 6 and 9. When $n_m = 6$, the six concentric loops have radii from 5 to 30 mm with a step size of 5 mm, whereas when $n_m = 9$, the nine concentric loops have radii from 10/3 to 30 mm with a step size of 10/3 mm. The observation points at the boundaries are selected at the points from $r = 1$ to 99 mm with a step size

of 1 mm, and for each observation point, the magnetic field inside or outside the SNP medium is estimated at $\Delta z = 1$ um away from the boundary surface.

After optimization based on Eq. (2), at $n_m = 6$, Fig. 3(a) shows the calculated B_r when a 0.1-A loop current is located at $z = -7$ mm (L_{in}) inside the SNP medium with both the SNP metasurface at the top and the auxiliary current loops at the bottom (the current direction in the figure indicates the original direction for the 0.1-A excitation current, but it will generate a field equivalent to a -0.1-A loop current in the free space because it is originally placed inside the SNP medium), and Fig. 3(b) shows the calculated B_r generated by a 0.1-A loop current located at $z = -13$ mm (L_{ext}) with both the SNP metasurface the auxiliary current loops. Besides, the fields in the ROI from both Figs. 3(a) and 3(b) are almost the same and are comparable to the reference, which is the field generated by a coaxial current loop placed 3 mm down the bottom of the ROI in the free space, as shown in Fig. 3(c). Figure 3(d) shows the field with the SNP metasurface only, and the field in the ROI is almost identical to that in Figs. 3(a) and 3(b) because, as stated previously, the fields generated by the auxiliary currents cancel those generated by L_{in} or L_{ext}. This implies that the proposed SNP metasurface facilitates the generation of magnetic fields in a region that is 17 mm away from the source (L_{in} case) where the distance can only be 3 mm without the SNP metasurface, a distance gain of $2D = 14$ mm. Considering the currents of the SNP metasurface at $z = 0$ mm, the proposed SNP metasurface gains a distance of $D = 7$ mm further away from the ROI. Moreover, in the ROI, a location
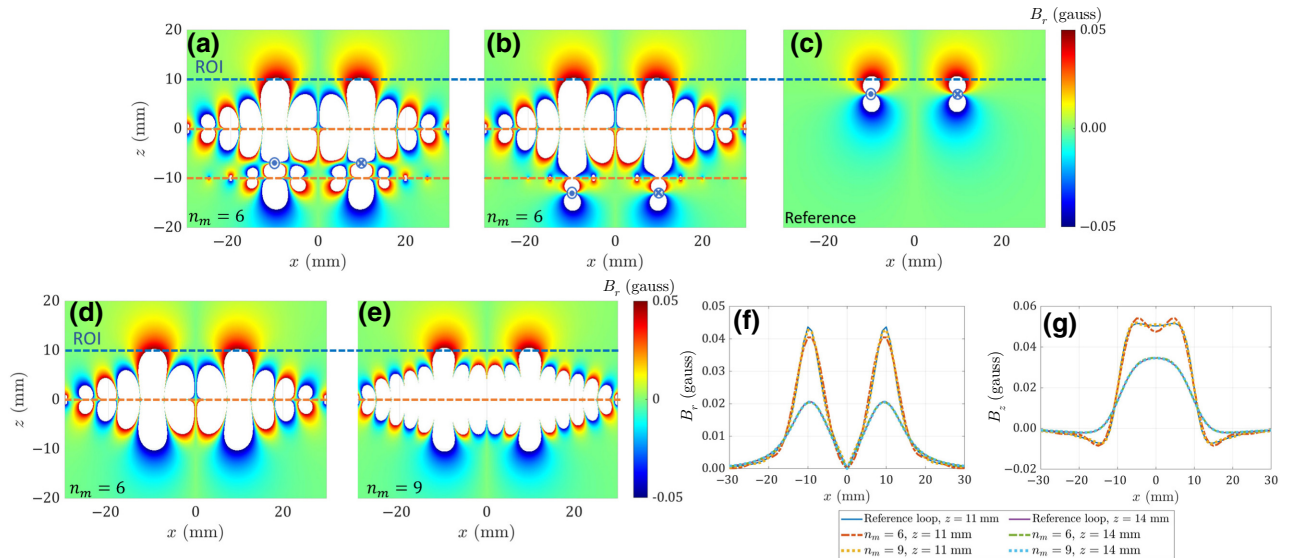

FIG. 3. Calculated B_r (a) generated by a 0.1-A loop current located at $z = -7$ mm (L_{in}) in the SNP medium with both the SNP metasurface and the auxiliary current loops, $n_m = 6$, (b) generated by a 0.1-A loop current located at $z = -13$ mm (L_{ext}) with both the SNP metasurface and the auxiliary current loops, $n_m = 6$, (c) generated by 0.1-A loop current located at $z = 7$ mm (L_{eq}), the reference case, (d) generated by the SNP metasurface only with $n_m = 6$, (e) generated by the SNP metasurface only with $n_m = 9$, (f) 1D field plots of B_r and (g) B_z.

TABLE I. Optimized current values for $n_m = 6$.

Loop radius (mm)	L_{in}		L_{ext}	
	Top-surface current (A)	Bottom-surface current (A)	Top-surface current (A)	Bottom-surface current (A)
5	-1.7091	-0.145	-1.7091	-0.0152
10	1.8674	0.3087	1.8674	-0.0417
15	-0.9767	-0.0845	-0.9767	-0.01
20	0.3647	0.0157	0.3647	-0.0033
25	-0.1268	-0.0052	-0.1268	0.0007
30	0.0256	-0.0001	0.0256	-0.0014

with a greater z has a closer field to that of the reference case.

Figure 3(e) shows the fields when n_m is set as 9. Comparing Figs. 3(c), 3(d), and 3(e), it is observed that a higher n_m value generates fields that are closer to the fields of the target reference. This is further confirmed by comparing the 1D field plots along the x axis, as shown in Figs. 3(f) and 3(g). Figures 3(f) and 3(g) show the calculated B_r and B_z along the x axis at $z = 11$ and 14 mm in the ROI, respectively. Notably, the accuracy is obtained at a price of higher input power as when n_m increases from 6 to 9, the current level in the SNP metasurface increases as shown in Tables I and II. This is because a larger n_m corresponds to a higher upper limit of the integration in Eq. (1), which leads to a higher current density. Although more current loops of the proposed SNP metasurface lead to fields closer to the desired ones, fewer loops are easier to implement and require lower current levels. Therefore, the value of n_m can be adjusted based on the accuracy requirements of a specific application.

For an experimental demonstration, to simplify the hardware setup and reduce the consumption of material, the proposed SNP metasurface is fabricated with $n_m = 6$ and the fields in the measurement region, $x = -28$ mm ~ 28 mm and $z = 11$ mm ~ 19 mm, in the ROI are measured. Figures 4(a) and 4(b) show the calculated B_r of the proposed SNP metasurface with $n_m = 6$ and that of the reference case in the measurement region, respectively. Figures 4(c), 4(d), 4(g), 4(h) show the corresponding measured

fields, and Figs. 4(e), 4(f), 4(i), 4(j) show the corresponding discrepancy between the measured and the analytical calculated results, which is $\Delta B = |B_{measured} - B_{calculated}|$. As shown in Figs. 4(c) and 4(d), in the measurement region, the measured fields agree well with the calculated results in Figs. 4(a) and 4(b). Therefore, the magnetic field generated by the designed SNP metasurface at $z = 0$ mm and that generated by a closer reference loop at $z = 7$ mm are comparable in the ROI. Figures 4(g) and 4(h) show the measured B_z of the two cases where they agree with each other as well.

To further illustrate the capability of the SNP metasurface, the same SNP metasurface in the experimental setup can be used to cancel the magnetic field from the reference loop (L_{eq}) in the ROI, renamed as the cancellation region, as shown in Fig. 5(a). Figure 5(b) shows the calculated $|\mathbf{B}|$ from the L_{eq} in the cancellation region (top layer), and the resulting magnetic field after we turn on the SNP metasurface to cancel it (bottom layer). It is clearly shown that the SNP metasurface can cancel the field generated by L_{eq}.

Moreover, extended from the case for only one excitation loop, the proposed SNP metasurface can be applied to displace multiple excitation loops when they are coaxial, as illustrated in Fig. 6(a). Applying the optimization algorithm to enforce the boundary condition based on Eq. (2), we can obtain the current values required for the SNP metasurface to displace each coaxial current loop in the SNP medium to the positions close to the ROI. The final SNP metasurface that displaces all excitation current

TABLE II. Optimized current values for $n_m = 9$.

| Loop radius (mm)	L_{in}		L_{ext}	
	Top-surface current (A)	Bottom-surface current (A)	Top-surface current (A)	Bottom-surface current (A)
10/3	8.9311	0.1562	8.9312	-0.0102
20/3	-10.7007	-0.3362	-10.7007	-0.0095
10	10.7891	0.5627	10.7891	-0.0391
40/3	-7.3655	-0.2292	-7.3655	-0.0024
50/3	3.8769	0.0555	3.8769	-0.0156
20	-1.8488	-0.0153	-1.8489	0.0114
70/3	0.7759	-0.0023	0.776	-0.0124
80/3	-0.2498	0.0045	-0.2498	0.0076
30	0.0418	-0.0028	0.0418	-0.0034
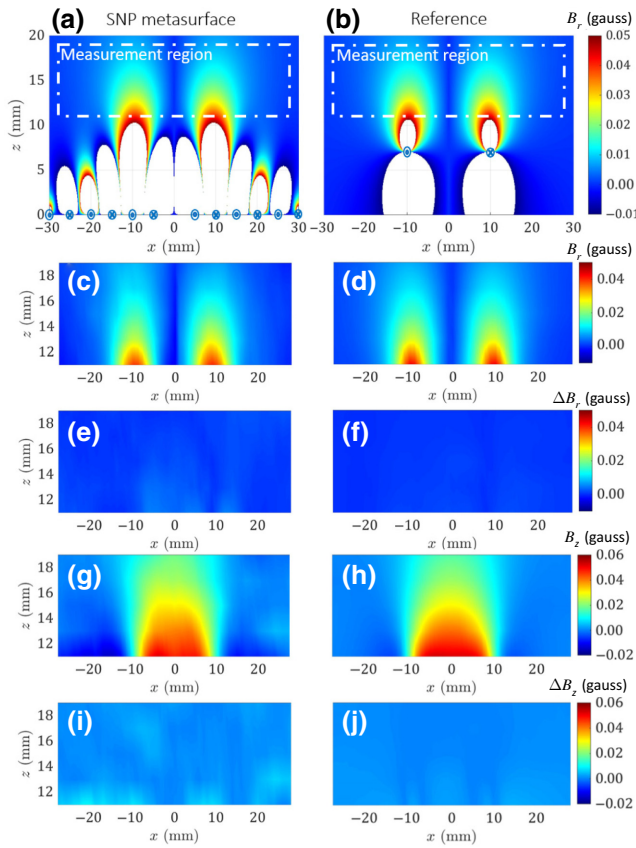
FIG. 4.   Calculated B_r (a) generated by the SNP metasurface with $n_m = 6$, (b) generated by the reference loop located at $z = 7$ mm (L_{eq}). Measured B_r (c),(d) and corresponding discrepancy compared with analytical calculated results (e),(f) in the measurement region for the SNP metasurface and reference loop. Measured B_z (g),(h) and corresponding discrepancy in (i),(j).

loops can be obtained by linearly combining the currents obtained for each excitation loop. Figures 6(b) and 6(c) show the calculated B_z in the ROI of a SNP metasurface designed for three coaxial current loops (running a current of 0.1 A) in a SNP medium centered at $(r, z) = (0, -6 \text{ mm}), (0, -7 \text{ mm})$, and $(0, -8 \text{ mm})$ with radii of 5,
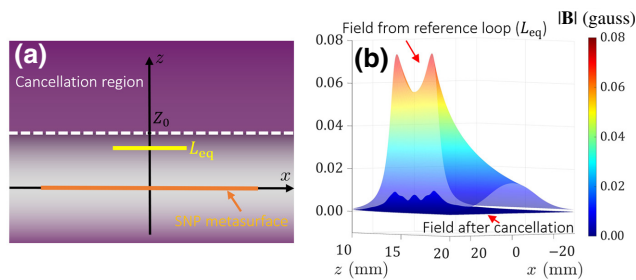

FIG. 5.   (a) Illustration on the principle for the SNP metasurface to cancel the field generated from the reference loop (L_{eq}). (b) |**B**| generated from L_{eq} and after cancellation with the SNP metasurface.
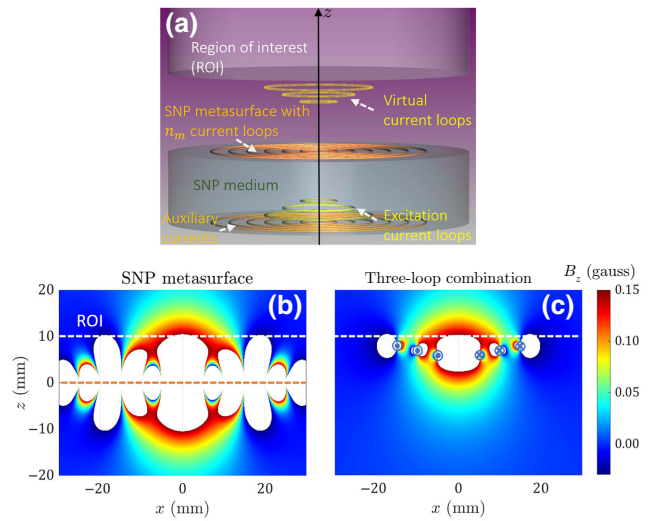

FIG. 6.   (a) Illustration of the proposed SNP metasurface extended to multiple coaxial excitation loops. Calculated B_z generated from (b) SNP metasurface and (c) three current loop combinations.

10, and 15 mm, and that of the three referenced current loops in the free space with the same current and radii centered at $(r, z) = (0, 6 \text{ mm}), (0, 7 \text{ mm})$, and $(0, 8 \text{ mm})$. They are comparable; thus, it is clearly shown that the SNP metasurface can transfer the three-loop combination in the SNP medium close to the ROI well.

Existing designs employ ferromagnetic and superconducting materials to experimentally fabricate the metamaterial used to guide the static magnetic field, such as the magnetic hose [19,20], magnetic concentrator [18], and magnetic cloaks [13,33]. The ROI must be surrounded by or in close contact with the metamaterial, which implies that if the ROI is not accessible, for instance, blocked by some obstacles, the designs cannot be applied or need to be changed. For the SNP metasurface proposed in this study, the ROI is far away from the surface and any nonmagnetic material nearby will not degrade the performance of the metasurface. Thus, the proposed SNP can be useful for applications such as drug delivery [4], nondestructive sensing of defects on soldering balls hidden beneath ball-grid array packages [34], tuning magnetic fields for MRI [8,9], and coil designs for transcranial magnetic stimulation [35].

In comparison with the structure proposed in Ref. [25], which can tailor the magnetic field in 2D, the proposed configuration can manipulate the field in 3D and has two advantages. One is the finite dimension for the virtual (reference) current loop on the transversal plane, which confines both the structure and the fields, and provides convenience to be applied at different places such as the human skin or surfaces of a region where magnetic fields are needed a distance away in the axial direction. The other is the simplicity of the design, where only a set of concentric surface current loops with negligible thickness far away

from the ROI is required to mimic a loop current and generate the same field pattern as if the loop current is near the ROI. Moreover, the working frequency for the proposed metasurface can be extended to the quasistatic range when the wavelength is much greater than the dimension of the metasurface.

III. CONCLUSION

In conclusion, we propose and experimentally demonstrate that a 2D SNP metasurface can displace dc magnetic fields generated by a coaxial loop current to a distant region. The results demonstrate that a 2D current distribution can gain the distance between a traditional current loop and the corresponding generated fields, which provides flexibility to control and transfer magnetic fields. The proposed approach can be used to transfer fields to regions where it is challenging to place a loop current nearby. Furthermore, it is shown that the design can be extended to more complicated excitation currents and can be further manipulated to switch off magnetic fields when needed. The proposed SNP metasurface is 2D and compact and can be pasted on surfaces to generate a magnetic field at a distant site going beyond nature. This ability, supported by a structure with a reduced dimension and with an increased degree of freedom for field control, provides more opportunities for drug delivery, designs of medical devices, measurement precision, etc.

ACKNOWLEDGMENTS

APPENDIX A: ANALYTICAL DERIVATION FOR THE SURFACE MAGNETIZATION CURRENT DENSITY ON THE SNP MEDIUM

Considering that,

$$\mathbf{B} = (\nabla \times \mathbf{A}), \tag{A1}$$

where **B** is the magnetic field (magnetic flux density), and **A** is the magnetic vector potential, with Coulomb gauge condition, we have

$$(\nabla \cdot \mathbf{A}) = 0, \tag{A2}$$

$$\nabla^2 \mathbf{A} = \nabla(\nabla \cdot \mathbf{A}) - \nabla \times (\nabla \times \mathbf{A}) = -\mu_m \mathbf{J}, \tag{A3}$$

where **J** is the free current density for the excitation current loops L_{in} or L_{ext} inside or outside the SNP medium, and μ_m is the magnetic permeability for the medium where the

excitation loops are placed in. Since $\mathbf{J} = J_\phi(r,z)\hat{\phi}$ in our problem, $\mathbf{A} = A_\phi(r,z)\hat{\phi}$, and at any position we have only

$$B_r = -\frac{\partial A_\phi}{\partial z}, B_z = \frac{1}{r}\frac{\partial(rA_\phi)}{\partial r}. \tag{A4}$$

To simplify the notation, we define the region above the SNP medium as the up region, and the region below the SNP medium as the down region. When the excitation is L_{in}, one has

$$(\nabla^2 - 1/r^2)A_\phi = \begin{cases} 0, & \text{in up and down regions} \\ -\mu_m J_\phi, & \text{in SNP region.} \end{cases} \tag{A5}$$

While when the excitation is L_{ext}, one has

$$(\nabla^2 - 1/r^2)A_\phi = \begin{cases} 0, & \text{in up and SNP regions} \\ -\mu_m J_\phi, & \text{in down region.} \end{cases} \tag{A6}$$

Next, the boundary conditions at the top and bottom surface of the SNP medium must be met, therefore,

$$B_{z-\text{in}} = B_{z-\text{out}}, \frac{B_{r-\text{in}}}{\mu_{\text{in}}} = \frac{B_{r-\text{out}}}{\mu_{\text{out}}}, \tag{A7}$$

where B_z and B_r denote the normal and tangential components of the **B**, the subscript in and out denote inside or outside the SNP medium. For the problem being solved, $\mu_{\text{in}} = -\mu_{\text{out}}$. Besides, $\mu_m = -\mu_0$ and μ_0 for L_{in} and L_{ext} excitation, respectively, and μ_0 is the free-space magnetic permeability.

By solving Eqs. (A5) and (A6) with the boundary conditions on the surface of the SNP medium, when the excitation is L_{in},

$$A_\phi^{\text{up}}(r,z) = \frac{\mu_0 I_e r_e}{2}\int_0^\infty e^{-(z-D)t}J_1(r_e t)J_1(rt)\,dt;$$

$$A_\phi^{\text{SNP}}(r,z) = \frac{\mu_0 I_e r_e}{2}\int_0^\infty (-e^{-|z+D|t} + e^{(z+D)t}$$
$$+ e^{-(z+D)t})J_1(r_e t)J_1(rt)\,dt;$$

$$A_\phi^{\text{down}}(r,z) = \frac{\mu_0 I_e r_e}{2}\int_0^\infty e^{(z+2Z_0-D)t}J_1(r_e t)J_1(rt)\,dt. \tag{A8}$$

Whereas when the excitation is L_{ext},

$$A_\phi^{\text{up}}(r,z) = \frac{\mu_0 I_e r_e}{2}\int_0^\infty e^{-(z-D)t}J_1(r_e t)J_1(rt)\,dt;$$

$$A_\phi^{\text{SNP}}(r,z) = \frac{\mu_0 I_e r_e}{2}\int_0^\infty e^{(z+D)t}J_1(r_e t)J_1(rt)\,dt;$$

$$A_\phi^{\text{down}}(r,z) = \frac{\mu_0 I_e r_e}{2}\int_0^\infty e^{-|z+2Z_0-D|t}J_1(r_e t)J_1(rt)\,dt. \tag{A9}$$

Based on Eq. (A4) and the expressions of A_ϕ^{SNP} in Eq. (A8), the surface magnetization current density for the L_{in} case can be derived as

$$\mathbf{K}_t^{\mathrm{in}}(r)\big|_{z=0} = M_r\big|_{z=0}\,\hat{r} \times \hat{z} = -\frac{2B_r}{\mu_0}\bigg|_{z=0}\hat{\phi}$$

$$= \frac{2\frac{\partial A_\phi^{\mathrm{SNP}}}{\partial z}}{\mu_0}\bigg|_{z=0}\hat{\phi} = I_e r_e \int_0^\infty e^{Dt} J_1(r_e t) J_1(rt) t\,dt\hat{\phi} \quad \text{(A10)}$$

$$\mathbf{K}_a^{\mathrm{in}}(r)\big|_{z=-Z_0} = M_r\big|_{z=-Z_0}\,\hat{r} \times -\hat{z}$$

$$= \frac{2B_r}{\mu_0}\bigg|_{z=-Z_0}\hat{\phi} = -\frac{2\frac{\partial A_\phi^{\mathrm{SNP}}}{\partial z}}{\mu_0}\bigg|_{z=-Z_0}\hat{\phi}$$

$$= I_e r_e \int_0^\infty e^{(Z_0-D)t} J_1(r_e t) J_1(rt) t\,dt\hat{\phi}, \quad \text{(A11)}$$

where M_r is the radial component of the magnetization field. Similarly, based on Eq. (A4) and the expressions of A_ϕ^{SNP} in Eq. (A9), the surface magnetization current density for the L_{ext} case can be derived as

$$\mathbf{K}_t^{\mathrm{ext}}(r)\big|_{z=0} = I_e r_e \int_0^\infty e^{Dt} J_1(r_e t) J_1(rt) t\,dt\hat{\phi}, \quad \text{(A12)}$$

$$\mathbf{K}_a^{\mathrm{ext}}(r)\big|_{z=-Z_0} = -I_e r_e \int_0^\infty e^{-(Z_0-D)t} J_1(r_e t) J_1(rt) t\,dt\hat{\phi}. \quad \text{(A13)}$$

It should be noted that $\mathbf{K}_t^{\mathrm{in}}(r)\big|_{z=0} = \mathbf{K}_t^{\mathrm{ext}}(r)\big|_{z=0} = \mathbf{K}_t(r)$, which means no matter where we place the excitation current loop, the top surface for the SNP metasurface always results in the same current density, and both of them have a divergent form. And $\mathbf{K}_t(r)$ oscillates in the r direction. Besides, for the bottom auxiliary surface current density, the $\mathbf{K}_a^{\mathrm{ext}}(r)\big|_{z=-Z_0}$ has a convergent form while $\mathbf{K}_a^{\mathrm{in}}(r)\big|_{z=-Z_0}$ still has a divergent form. Moreover, when the value of D approaches 0, the expression for $\mathbf{K}_t(r)$ approximates to

$$\mathbf{K}_t(r) \approx I_e r_e \int_0^\infty t J_1(r_e t) J_1(rt)\,dt\hat{\phi}$$

$$= I_e r_e \frac{\delta(r-r_e)}{r_e}\hat{\phi} = I_e \delta(r-r_e)\hat{\phi}, \quad \text{(A14)}$$

which is equivalent to the excitation current loop with current I_e at $z=0$. And the SNP metasurface does not gain any distance to generate a magnetic source remotely at all. While when D increases and approaches the value of Z_0, the surface current density increases exponentially due to the component e^{Dt} in the integration expression for $\mathbf{K}_t(r)$,

which means more current level and power is needed if we want to push the virtual loop further in the positive z direction.

Moreover, although $\mathbf{K}_t(r)$ diverges, we can truncate the integration to obtain a good approximation of the magnetic vector potential and thus the magnetic field in the ROI. Following is the reasoning. If we truncate $K_t(r)$ by setting the upper limit of the integration to a finite number c, $K_t(r)$ is re-expressed as $K_t'(r)$:

$$K_t'(r) = I_e r_e \int_0^c e^{Dt} J_1(r_e t) J_1(rt) t\,dt. \quad \text{(A15)}$$

In Eq. (A15), it is noted that greater c is, more oscillations $K_t(r)$ has in the r direction. Based on Eq. (A15), the magnetic vector potential generated by $K_t'(r)$ in the up region (i.e., the region above the SNP medium) can be derived as

$$A_\phi^{\mathrm{up}K'}(r,z)$$

$$= \frac{\mu_0}{2}\int_0^\infty K_t'(r')r' \int_0^\infty e^{-zt'} J_1(r't') J_1(rt')\,dt'\,dr', \quad \text{(A16)}$$

where r' is the radial position of the surface current density $K_t'(r')$ at $z=0$, and (r,z) is the coordinate of the observation point in the up region. By substituting Eq. (A15) into Eq. (A16), one has

$$A_\phi^{\mathrm{up}K'}(r,z) = \frac{\mu_0 I_e r_e}{2}\int_0^c e^{-(z-D)t} J_1(r_e t) J_1(rt)\,dt. \quad \text{(A17)}$$

Equation (A17) is the expression of the magnetic vector potential in the up region when $K_t(r)$ is truncated.

Visiting the original expressions for the magnetic vector potential in the up region, $A_\phi^{\mathrm{up}}(r,z)$, in Eqs. (A8) and (A9), it is noted that in the ROI ($z > Z_0$ and thus $z > D$), the integration with respect to t can be truncated due to the exponential loss term $e^{-(z-D)t}$. It means that in the original solutions, the magnetic vector potential in the ROI can be estimated using an integration with a finite value as the upper limit, and so is the magnetic field in the ROI. Therefore, $A_\phi^{\mathrm{up}}(r,z)$ can be approximated using $A_\phi^{\mathrm{up}K'}(r,z)$ with truncated $K_t(r)$. In other words, by truncating the $K_t(r)$ to $K_t'(r)$, we can still reassemble the dominant components of $A_\phi^{\mathrm{up}}(r,z)$ in the ROI, and it validates the implementation of the proposed SNP metasurface. The higher the upper limit of the integration in Eq. (A15), the closer the fields are to the idea situation (the reference case where a current loop is at the L_{eq} location in the free space), and with the expense of higher current density and more oscillations along the radial direction. Besides, when z increases, the exponential loss term $e^{-(z-D)t}$ decreases faster, which means that the field is closer to the reference case at a location with a larger z value in the ROI. This is reflected in Fig. 5(b), which shows that the cancellation is more complete when z increases.
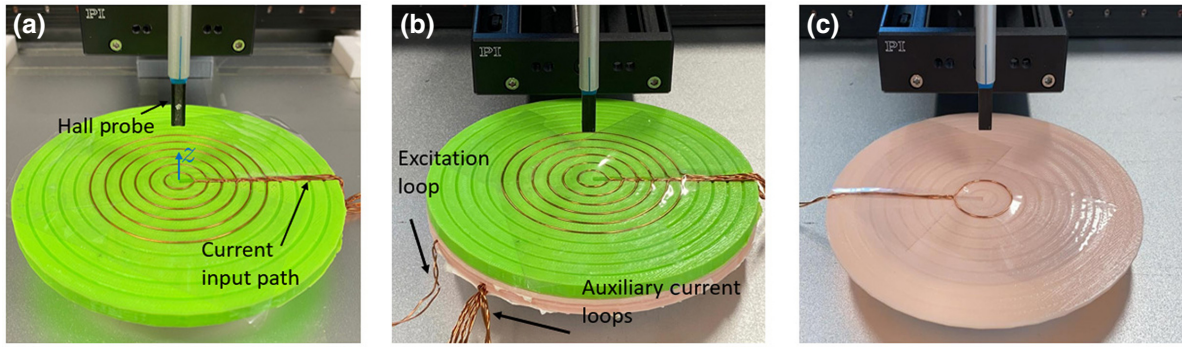
FIG. 7. Physical implementation of (a) the SNP metasurface only, (b) with the excitation loop and the auxiliary current loops and (c) reference loop only for experimental demonstration.

APPENDIX B: DETAILS OF NUMERICAL OPTIMIZATION

As the magnetic field in the whole space can be transformed to the summation of the field generated by the $\mathbf{K}_t(r)$, $\mathbf{K}_a(r)$ and the excitation loop L_{in} or L_{ext} in the free space (it should be noted that when the excitation loop is L_{in}, it will generate a magnetic field in the free space, which is equivalent to that generated by a loop with opposite current value since it is originally placed in the SNP medium). The optimization is aimed to minimize the error on the boundaries of the SNP medium for the field generated by the SNP metasurface, auxiliary current loops and the excitation loop L_{in} or L_{ext}. Besides, the normal component of the magnetic field generated from these current sources fulfills the boundary condition directly, thus the optimization is mainly aimed to satisfy the boundary condition for the tangential component of the magnetic field based on Eq. (A7).

The target function to minimize the error for the tangential components is stated as Eq. (2). In addition, the optimization was done by MATLAB software using the fmincon function, all the current values in the top and bottom surface of the SNP medium are set to 0 at the starting point. Considering that the boundary condition on the top surface of the SNP medium is purely dependent on the current at the excitation position and the bottom-surface auxiliary current loops, and the boundary condition on the bottom surface of the SNP medium is purely dependent on the current at the excitation position and the top-surface SNP metasurface current loops. One can separate the optimization into two parts to obtain the current values on the top and bottom surface of the SNP medium separately to save the optimization time. Therefore, the two target residual functions to minimize are

$$f_{\text{top}} = \sum_{j=1}^{n_c/2} \left(\sum_{i=1}^{n_m+1} \frac{B_{t-\text{in}}^{ij}}{\mu_{\text{in}}} - \sum_{i=1}^{n_m+1} \frac{B_{t-\text{out}}^{ij}}{\mu_{\text{out}}} \right)^2, \qquad (B1)$$

$$f_{\text{bottom}} = \sum_{j=1}^{n_c/2} \left(\sum_{i=1}^{n_m+1} \frac{B_{t-\text{in}}^{ij}}{\mu_{\text{in}}} - \sum_{i=1}^{n_m+1} \frac{B_{t-\text{out}}^{ij}}{\mu_{\text{out}}} \right)^2, \qquad (B2)$$

where f_{top} is used to obtain the current value for the bottom-surface auxiliary current loops to satisfy the boundary condition on the top surface, while f_{bottom} is used to obtain the current value for the top-surface current loops to satisfy the boundary condition on the bottom surface.

The optimized current values are shown in Tables I and II, respectively. It should be noted that when the excitation loop is placed at L_{in} or L_{ext} position, the top surface has almost the same current discretization, which is expected from the analytical derivation results for the surface-magnetization current density from Eq. (A10) and (A12). While for the bottom-surface current discretization, when the excitation is at L_{ext} position, the current discretization has a similar pattern compared with the expression in Eq. (A13), which is different from the current discretization for the L_{in} excitation. Moreover, the top-surface current level increases when n_m increases from 6 to 9. This is because when n_m increases, the upper limit for the integration range in Eqs. (A10) and (A12) is increased and thus the current density is amplified. And this higher integration range leads to a closer field pattern to that of the reference case as shown in Fig. 3.

APPENDIX C: EXPERIMENTAL SETUP AND SUPPLEMENTAL MEASUREMENT RESULTS

Figure 7(a) shows the physical implementation of the designed SNP metasurface, Fig. 7(b) shows the physical implementation of the designed SNP metasurface together with the excitation loop L_{in} and the auxiliary current loops at the bottom, and Fig. 7(c) shows the reference case, a current loop in the air. The 3D-printed material used to support these current loops is polylactic acid (PLA), which is nonmagnetic and has negligible influence on the static
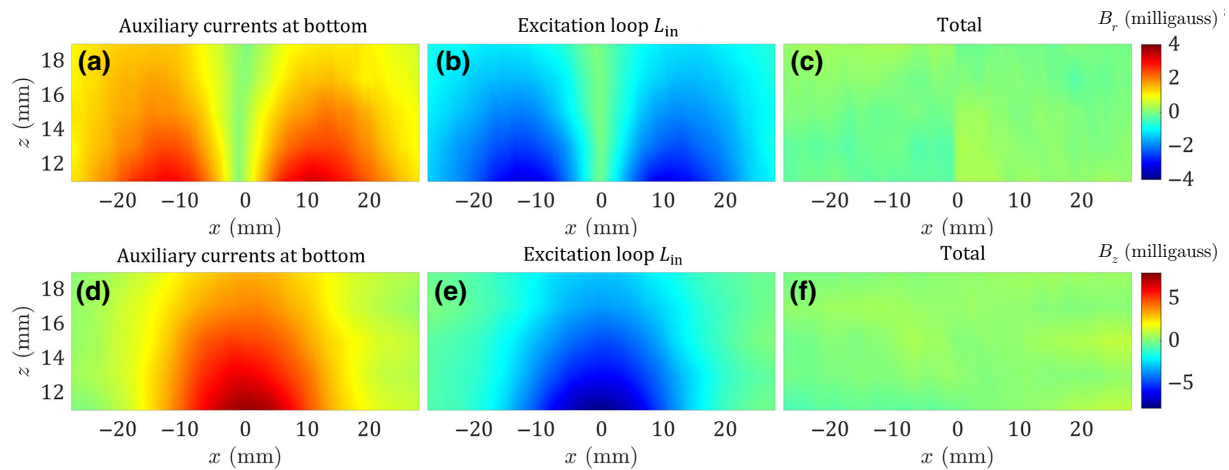
FIG. 8. Practical measured B_r and B_z components for the bottom-surface auxiliary loops, the excitation loop, and the summation of them.

field measurements. A Hall probe (LakeShore 460 Gauss-meter) positioned at a PI (Physik Instrumente) xyz-moving platform (VT-80 linear stage) is used to measure the B_z and B_r components of the magnetic field. Additionally, two Keysight E3632A, one Keysight U8031A and one Keysight N6705C dc power supplies are used to precisely control the current value in different loops. Besides, before tuning on the power supplies, the background magnetic field (such as the earth magnetic field) is measured first and then subtracted from the measurement results when the power supplies are turned on to improve the measurement accuracy. Moreover, the probe tip is swept in the plane, which is perpendicular to the current input path to avoid the possible field distortion caused by the current input path.

Next, the cancellation of the magnetic fields generated by the auxiliary currents at the bottom and that of the excitation current loop is experimentally validated. Figures 8(a) and 8(d), respectively, show the measured B_r and B_z generated by the auxiliary current loops in the measurement region. And Figs. 8(b) and 8(e) show the measured B_r and B_z generated by the excitation loop L_{in} in the measurement region. Next, Figs. 8(c) and 8(f) show the summation of the field generated from the auxiliary current loops and the excitation loop, and they validate that in the ROI (or the measurement region), the field from the auxiliary currents at the bottom and that of the excitation current loop can cancel with each other. Moreover, it should be noted that since the excitation loop L_{in} is originally placed within the SNP medium, the current value inside it needs to turn to opposite in the measurement. Besides, to further ensure that the measured field is far away from the probe and surrounding noise, the current level for the SNP metasurface is increased by a factor of 2 in the real measurement and the measurement results shown in this paper are processed from the practical results divided by 2. For the auxiliary bottom-surface current loops measurement, the factor is

10. While for the reference loop L_{eq} and the excitation loop L_{in} measurements, the factor is 50.

[1] T. d. P. M. Bazzo, J. F. Kölzer, R. Carlson, F. Wurtz, and L. Gerbaud, Multiphysics design optimization of a permanent magnet synchronous generator, IEEE Trans. Ind. Electron. **64**, 9815 (2017).

[2] J. Pfeiffer, P. Kuester, I. E. Schulz, J. Friebe, and P. Zacharias, Review of flux interaction of differently aligned magnetic fields in inductors and transformers, IEEE Access **9**, 2357 (2020).

[3] Y. Xie, Z. Zhang, Y. Lin, T. Feng, and Y. Xu, Magnetic Quasi-Bound State in the Continuum for Wireless Power Transfer, Phys. Rev. Appl. **15**, 044024 (2021).

[4] K. Wu, D. Su, J. Liu, R. Saha, and J.-P. Wang, Magnetic nanoparticles in nanomedicine: A review of recent advances, Nanotechnology **30**, 502003 (2019).

[5] C. Navau, R. Mach-Batlle, A. Parra, J. Prat-Camps, S. Laut, N. Del-Valle, and A. Sanchez, Enhancing the sensitivity of magnetic sensors by 3D metamaterial shells, Sci. Rep. **7**, 1 (2017).

[6] R. Mach-Batlle, C. Navau, and A. Sanchez, Invisible magnetic sensors, Appl. Phys. Lett. **112**, 162406 (2018).

[7] O. Veiseh, J. W. Gunn, and M. Zhang, Design and fabrication of magnetic nanoparticles for targeted drug delivery and imaging, Adv. Drug Deliv. Rev. **62**, 284 (2010).

[8] Z. H. Ren, W. C. Mu, and S. Y. Huang, Design and optimization of a ring-pair permanent magnet array for head imaging in a low-field portable MRI system, IEEE Trans. Magn. **55**, 1 (2018).

[9] Z. H. Ren, J. Gong, and S. Y. Huang, An irregular-shaped inward-outward ring-pair magnet array with a monotonic field gradient for 2D head imaging in low-field portable MRI, IEEE Access **7**, 48715 (2019).

[10] J. B. Pendry, D. Schurig, and D. R. Smith, Controlling electromagnetic fields, Science **312**, 1780 (2006).

[11] S. Narayana and Y. Sato, dc magnetic cloak, Adv. Mater. 24, 71 (2012).

[12] J. Prat-Camps, A. Sanchez, and C. Navau, Superconductor–ferromagnetic metamaterials for magnetic cloaking and concentration, Supercond. Sci. Technol. 26, 074001 (2013).

[13] J. Zhu, W. Jiang, Y. Liu, G. Yin, J. Yuan, S. He, and Y. Ma, Three-dimensional magnetic cloak working from dc to 250 KHz, Nat. Commun. 6, 1 (2015).

[14] W. Jiang, Y. Ma, and S. He, Static Magnetic Cloak Without a Superconductor, Phys. Rev. Appl. 9, 054041 (2018).

[15] C. Navau, J. Prat-Camps, and A. Sanchez, Magnetic Energy Harvesting and Concentration at a Distance by Transformation Optics, Phys. Rev. Lett. 109, 263903 (2012).

[16] F. Sun and S. He, Static magnetic field concentration and enhancement using magnetic materials with positive permeability, Prog. Electromagn. Res. 142, 579 (2013).

[17] F. Sun and S. He, dc magnetic concentrator and omnidirectional cascaded cloak by using only one or two homogeneous anisotropic materials of positive permeability, Prog. Electromag. Res. 142, 683 (2013).

[18] K. Liu, W. Jiang, F. Sun, and S. He, Experimental realization of strong dc magnetic enhancement with transformation optics, Prog. Electromagn. Res. 146, 187 (2014).

[19] C. Navau, J. Prat-Camps, O. Romero-Isart, J. I. Cirac, and A. Sanchez, Long-Distance Transfer and Routing of Static Magnetic Fields, Phys. Rev. Lett. 112, 253901 (2014).

[20] P. Zhou, G. Ma, H. Liu, X. Li, H. Zhang, C. Yang, and C. Ye, Transportation of static magnetic fields by a practically realizable magnetic hose, IEEE Magn. Lett. 7, 1 (2015).

[21] J. Prat-Camps, C. Navau, and A. Sanchez, A magnetic wormhole, Sci. Rep. 5, 1 (2015).

[22] F. Sun and S. He, Transformation magneto-statics and illusions for magnets, Sci. Rep. 4, 1 (2014).

[23] R. Mach-Batlle, A. Parra, S. Laut, N. Del-Valle, C. Navau, and A. Sanchez, Magnetic Illusion: Transforming a Magnetic Object into Another Object by Negative Permeability, Phys. Rev. Appl. 9, 034007 (2018).

[24] R. Mach-Batlle, A. Parra, S. Laut, C. Navau, N. Del-Valle, and A. Sanchez, in *2017 11th International Congress on Engineered Materials Platforms for Novel Wave Phenomena (Metamaterials)* (IEEE, Marseille), p. 301.

[25] R. Mach-Batlle, M. G. Bason, N. Del-Valle, and J. Prat-Camps, Tailoring Magnetic Fields in Inaccessible Regions, Phys. Rev. Lett. 125, 177204 (2020).

[26] M. J. Freire, R. Marques, and L. Jelinek, Experimental demonstration of a $\mu = -1$ metamaterial lens for magnetic resonance imaging, Appl. Phys. Lett. 93, 231108 (2008).

[27] K. Sun, R. Fan, Z. Zhang, K. Yan, X. Zhang, P. Xie, M. Yu, and S. Pan, The tunable negative permittivity and negative permeability of percolative Fe/Al_2O_3 composites in radio frequency range, Appl. Phys. Lett. 106, 172902 (2015).

[28] R. Mach-Batlle, A. Parra, J. Prat-Camps, S. Laut, C. Navau, and A. Sanchez, Negative permeability in magnetostatics and its experimental demonstration, Phys. Rev. B 96, 094422 (2017).

[29] G. W. Milton, N.-A. P. Nicorovici, R. C. McPhedran, and V. A. Podolskiy, A proof of superlensing in the quasistatic regime, and limitations of superlenses in this regime due to anomalous localized resonance, Proc. R. Soc. A: Math., Phys. Eng. Sci. 461, 3999 (2005).

[30] R. C. McPhedran and G. W. Milton, A review of anomalous resonance, its associated cloaking, and superlensing, C. R. Phys. 21, 409 (2020).

[31] J. Jeans, in *Mathematical Theory of Electricity and Magnetism* (Cambridge University Press, Cambridge, England, 2009), 5th ed., p. 156–184.

[32] S. Hampton, R. Lane, R. Hedlof, R. Phillips, and C. A. Ordonez, Closed-form expressions for the magnetic fields of rectangular and circular finite-length solenoids and current loops, AIP Adv. 10, 065320 (2020).

[33] F. Gömöry, M. Solovyov, J. Šouc, C. Navau, J. Prat-Camps, and A. Sanchez, Experimental realization of a magnetic cloak, Science 335, 1466 (2012).

[34] X. Zhou, X. Lu, X. Cao, Z. Liu, and Y. Chen, Research on life evaluation method of solder joint based on eddy current pulse thermography, Rev. Sci. Instrum. 90, 084901 (2019).

[35] Z.-D. Deng, S. H. Lisanby, and A. V. Peterchev, Electric field depth–focality tradeoff in transcranial magnetic stimulation: Simulation comparison of 50 coil designs, Brain Stimul. 6, 1 (2013).